WATER RESOURCES RESEARCH, VOL. 36, NO. 5, PAGES 1165–1177, MAY 2000

Flow in unsaturated fractured porous media: Hydraulic conductivity of rough surfaces

Dani Or and Markus Tuller

Department of Plants, Soils, and Biometeorology, Utah State University, Logan

Abstract. The general trend in models for flow in unsaturated fractured porous media is to regard desaturated fractures as nonparticipating elements that impede flow. Mounting experimental and theoretical evidence shows that fractures retain and conduct liquid in the form of film and partially filled corner flow to a relatively low degree of saturation. A simple geometrical model for rough fracture surfaces is developed offering a tractable geometry for calculations of surface liquid storage due to adsorbed films and capillary menisci. Assuming that under slow laminar flow the equilibrium liquid configurations on the fracture surface are not modified significantly, the average hydraulic conductivities for film and corner flows were derived and used as building blocks for a representative fracture roughness element and an assemblage of statistically distributed surface roughness elements. Calculations for a single representative element yielded excellent agreement with surface storage and unsaturated hydraulic conductivity measurements of *Tokunaga and Wan* [1997]. A statistical representation of surface roughness using a gamma distribution of pit depths resulted in closed-form expressions for unsaturated hydraulic conductivity averaged across the fracture length (transverse to flow) or weighted by the liquid cross section occupying the fracture surface. An important attribute of the surface roughness model is the direct link between fracture surface and matrix processes unified by the matric potential. The proposed model represents a first step toward development of a comprehensive approach for liquid retention and hydraulic conductivity of unsaturated fractured porous media based on details of liquid configuration for different matric potentials.

1. Introduction

The large disparity in hydraulic behavior between fractures and matrix in unsaturated fractured porous media (FPM) presents practical and theoretical challenges to modeling of total system response [*Glass et al.*, 1995]. Naturally fractured porous media consist of interconnected fracture and pore networks forming two distinct pore spaces (in some cases, multiple continua are considered [*Pruess and Narasimhan*, 1982]). Large pores and crevices (10^{-4}–10^{-2} m [*Tsang and Tsang*, 1987; *Fischer et al.*, 1998]) are often associated with fractures, and a system of much smaller pores (10^{-7}–10^{-5} m [*Thoma et al.*, 1992]) is associated with the porous matrix. Although fractures are generally considered fast transport pathways [*Zimmerman and Bodvarsson*, 1996], under partial saturation fractures can impede flow [*Wang and Narasimhan*, 1985]. As saturation decreases, wide aperture fractures drain first when bulk liquid is displaced by a gaseous or a nonwetting phase. However, the wetting phase is not completely displaced, as some liquid remains adsorbed on surfaces in the form of films or held by capillary forces in crevices, asperities, and pits on rough fracture surfaces [*Wang and Narasimhan*, 1985; *Glass et al.*, 1995]. Some aperture-based conceptual models assume that such empty fractures do not participate in flow except at a few contact areas [*Wang and Narasimhan*, 1985] or only through a network of locally saturated channels [*Tsang and Tsang*, 1987] and wedges [*Rasmussen*, 1987]. However, recent evidence shows that film and groove flow along (unbridged) fracture surfaces is a potentially important transport mechanism under partial fracture saturation [*Tokunaga and Wan*, 1997]. The practical significance of such a transport mechanism and its contribution to overall FPM permeability is a matter of ongoing debate. In a recent study, *Pruess* [1999] concluded that the potential contribution to FPM permeability of flow on rough fracture surfaces (represented by vertical half capillaries) under the matric potential conditions prevailing in Yucca Mountain (~−3 bars) is likely to be small.

Modeling liquid retention and flow in grooves and films is sensitive to surface roughness characteristics. Experiments conducted by *Rye et al.* [1996] on flow in open V-shaped surface grooves showed strong dependence of flow rates on groove angle and solid-liquid contact angle. Theoretical analyses of *Philip* [1978] and *Novy et al.* [1989] demonstrated the significance of surface roughness geometry on liquid adsorption and capillary condensation. A numerical method based on the boundary integral formulation for Stokes flow was introduced by *Pozrikidis* [1988] to analyze the flow of liquid films along rough surfaces. Experimental data for flow along rough fracture surfaces were presented by *Fourar et al.* [1993] and more recently by *Tokunaga and Wan* [1997].

The objective of this study was to develop a model for flow on rough surfaces of unsaturated fractures based on hydrostatic liquid configuration due to adsorptive and capillary forces. This is a first step toward developing a framework for liquid retention and hydraulic conductivity in partially saturated fractured porous media that combines realistic models of matrix and fracture pore space geometry and explicitly considers the roles of adsorption, capillarity, and hydrodynamic processes in such pore geometry. The basis for the proposed hydrodynamic modeling of flow in thin liquid films and surface

Copyright 2000 by the American Geophysical Union.

Paper number 2000WR900020.
0043-1397/00/2000WR900020$09.00

9806

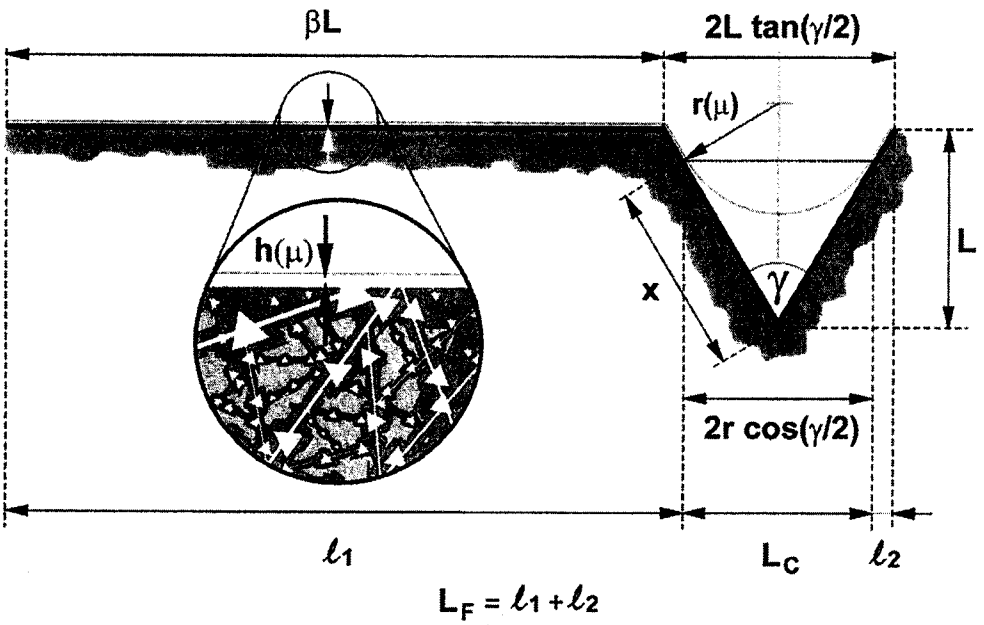

Figure 1. Definition sketch for a unit element representing unsaturated fracture surface with a single pit of depth L and angle γ. Liquid-vapor interfaces are functions of the matric potential μ, which determines the radius of curvature in the pit $r(\mu)$ and film thickness $h(\mu)$. The inset represents the partially saturated porous rock matrix forming the fracture; water in the rock matrix pore space is in equilibrium with water on the fracture surface.

grooves at various matric potentials was the equilibrium liquid-vapor interfacial configuration. For slow laminar flow these interfaces are considered stable and thus provide the necessary boundary conditions for the Navier-Stokes equations in the assumed geometry. A statistical distribution of an elementary roughness element is introduced to characterize fracture surface roughness. Model calculations for various surface geometries are presented and compared with experimental data published by *Tokunaga and Wan* [1997]. Detailed analytical solutions for average hydraulic fracture surface conductivity are presented.

2. Theoretical Considerations

Thermodynamic considerations for adsorbed film thickness and capillary-dependent interface curvature are combined to obtain a detailed picture of liquid-vapor interfaces under hydrostatic equilibrium [*Tuller et al.*, 1999; *Or and Tuller*, 1999]. Various types of long- and short-range surface forces induce liquid adsorption as films on solid surfaces [*Derjaguin et al.*, 1987]; additional volumes of liquid are held in crevices and pits by capillary forces. Equilibrium liquid-vapor interfacial configurations as a function of matric potential provide well-defined boundaries for the introduction of hydrodynamic considerations. The underlying assumption is that for slow laminar flow regimes, these liquid configurations and interfaces remain relatively stable. These simplifications provide the starting point for developing a model for average unsaturated hydraulic conductivity of rough fracture surfaces.

2.1. Fracture Surface Geometry

The cross-sectional profile of surface roughness of a relatively wide fracture is represented by an assemblage of individual roughness elements with cross-sectional geometry as depicted in Figure 1. (A similar roughness geometry was used by *Colbeck* [1996] to study capillary adhesion of grooved surfaces.) Each roughness element contains a groove or an isolated pit attached to an essentially flat surface segment (more generally, to a surface segment with roughness much smaller than pit depth L). Pit geometry is defined by its depth L, an angle γ, and by pit spacing βL. The nondimensional parameter β defines the pit/groove density per unit fracture surface, assumed to be proportional to pit depth L.

The fracture aperture is assumed to be sufficiently wide to preclude fracture snap-off (spontaneous filling of the gap or the entire aperture) at all matric potentials and flow rates under consideration. The extension of the analysis to fully saturated fractures is simple for a known aperture size (or a distribution of aperture sizes). In assembling the unsaturated hydraulic conductivity for the rough surface, we consider the individual contributions of film and groove (corner) flows to the total flow on the fracture surface. If fracture surface roughness is primarily in the form of isolated pits, the dominating hydraulic regime is expected to be in the form of liquid film flow. In the presence of an appreciable number of continuous grooves most of the flow is expected to be conducted as "corner" flow [*Ransohoff and Radke*, 1988; *Dullien et al.*, 1986]. Under most realistic conditions, flow on unsaturated fracture surfaces is likely to be a result of these two processes.

2.2. Liquid Retention in a Surface Roughness Element

The ability to describe the amount of liquid retained and the configuration of liquid-vapor interfaces is key to subsequent calculations of hydraulic conductivity. The thickness (h) of a liquid film adsorbed on a planar surface and confined by a vapor phase may be calculated as a function of matric potential (μ) as [*Iwamatsu and Horii*, 1996]

$$h(\mu) = \sqrt[3]{\frac{A_{svl}}{6\pi\rho\mu}}, \tag{1}$$

where A_{svl} is the Hamaker constant for solid-vapor interactions through the intervening liquid and ρ is the density of the liquid. The matric potential is expressed in terms of energy per unit mass [J kg^{-1}] and may be converted to pressure (energy/volume) [Pascals] by multiplication by water density (ρ). Equation (1) represents the simplest form of liquid adsorption on solid surfaces considering van der Waals forces only [*Derjaguin et al.*, 1987]. The total amount of liquid associated with films is determined not only by the area of the film of the flat segment, $\beta L h(\mu)$, but also by films exposed on the pit/groove surfaces as the radius of curvature decreases and liquid recedes deeper into the groove (Figure 1). To calculate these additional film surfaces, we need first to discuss liquid retention by capillary forces.

The radius of liquid-vapor interface curvature (r) for unsaturated conditions is dependent on matric potential (μ) according to the Young-Laplace relationship:

$$r(\mu) = -\frac{\sigma}{\rho\mu}, \tag{2}$$

where σ is the surface tension of the liquid. An interesting feature of this uniform capillary radius of curvature is that all grooves with an angle γ retain the same amount of liquid-filled cross-sectional area regardless of the groove's depth (L). The amount of liquid retained in a corner A_C (expressed in this analysis as cross-sectional area) is given by (Figure 2)

$$A_C(\mu) = r(\mu)^2 F(\gamma), \tag{3}$$

where $F(\gamma)$ is pit angularity factor defined as [*Tuller et al.*, 1999]

$$F(\gamma) = \frac{1}{\tan(\gamma/2)} - \frac{\pi(180-\gamma)}{360}. \tag{4}$$

With the liquid cross-sectional area associated with capillarity defined, we may now calculate the cross-sectional film area $A_F(\mu)$ as (see Figure 1)

$$A_F(\mu) = h(\mu)\left\{\beta L + 2\left[\frac{L}{\cos(\gamma/2)} - \frac{r(\mu)}{\tan(\gamma/2)}\right]\right\}, \tag{5}$$

where $h(\mu)$ is the thickness of the adsorbed film (equation (1)) and $r(\mu)$ is the radius of interface curvature (equation (2)).

When the curved liquid-vapor interface reaches the pit edge, the pit is considered completely filled, and no further increase of interface curvature is possible (i.e., a "jump" to a flat liquid-vapor interface is assumed). The relationships between pit geometry and the critical matric potential μ_c at this point are defined by

$$\mu_c = -\frac{\sigma\cos(\gamma/2)}{\rho L\tan(\gamma/2)}, \tag{6}$$

and the critical radius of curvature is simply $r_c(\mu_c) = [L\tan(\gamma/2)]/[\cos(\gamma/2)]$.

2.3. Flow in Thin Liquid Films Adsorbed on Fracture Surfaces

The flow velocity distribution normal to film cross section is obtained from a solution of the following simplified Navier-Stokes equation [*Spurk*, 1997]:

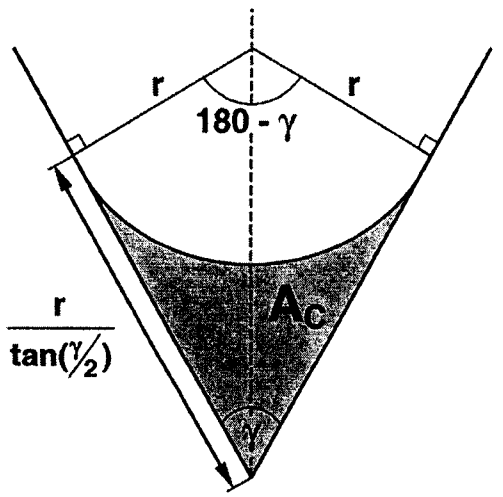

Figure 2. Liquid-vapor interfacial configuration and liquid-filled cross-sectional area in a corner.

$$-\frac{dP}{dz} = \eta_0\frac{d^2v}{dy^2}, \tag{7}$$

where v is the velocity, y is the distance taken normal to the solid surface, dP/dz is the hydraulic gradient in flow direction z, and η_0 is the viscosity of bulk liquid. Double integration of (7) yields the velocity profile normal to the solid surface:

$$v(y) = \frac{y^2 - 2hy}{2\eta_0}\left(-\frac{dP}{dz}\right). \tag{8}$$

The velocity profile (equation (8)) may be integrated again and divided by film thickness (h) to yield an average liquid velocity for a given matric potential:

$$\bar{v} = \frac{h^2(\mu)}{3\eta_0}\left(-\frac{dP}{dz}\right). \tag{9}$$

This expression relates the film thickness h (equation (1)) as a function of the matric potential μ and the mean velocity and is valid only when the liquid viscosity is constant throughout the film. Experimental and theoretical evidence shows a presence of a thin layer with modified viscosity close to the solid surface. Liquid viscosity is elevated relative to bulk liquid because of short- and long-range interfacial forces [*Low*, 1976, 1979; *Derjaguin et al.*, 1987; *McBride and Baveye*, 1995]. Expressions derived by *Low* [1979] for viscosity profiles of water altered by interfacial forces were recently modified by *Or and Wraith* [1999] to represent viscosity in terms of distance from the solid surface:

$$\eta(y, T) = \eta_0\exp\left(\frac{a^*}{yT}\right), \tag{10}$$

where y is the distance from the solid surface (angstroms), T is temperature (Kelvins), and $a^* = 1621$ (Å K) is a constant modified from *Low* [1979]. While these relationships are not universal, they provide a first approximation for the effect of surface forces on liquid viscosity. Substituting (10) into (7) and performing the integrations yields an expression for average velocity considering effects of modified liquid viscosity near solid surfaces:

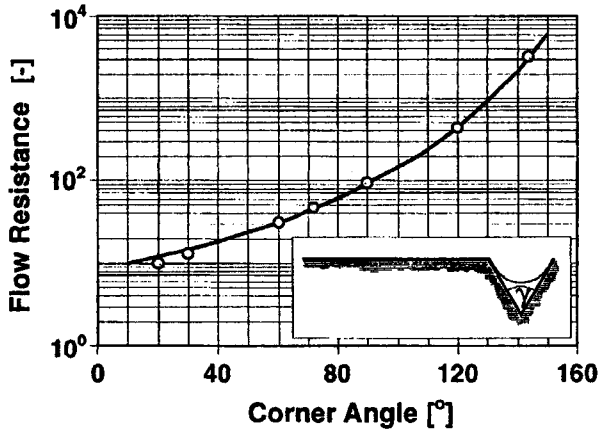

Figure 3. Nondimensional corner resistance to flow as a function of corner angle γ calculated from tabulated values of *Ransohoff and Radke* [1988].

$$\bar{v} = \frac{B(\mu)}{12\eta_0 h(\mu)}\left(-\frac{dP}{dz}\right), \tag{11}$$

with the function $B(\mu)$ for a given film thickness $h(\mu)$:

$$B(\mu) = (4h(\mu)^3 - 5ah(\mu)^2 - a^2h(\mu)) \exp\left(-\frac{a}{h(\mu)}\right) - (6a^2h(\mu) + a^3)\ \mathrm{Ei}\left[-\frac{a}{h(\mu)}\right]$$

where $\mathrm{Ei}[x] = \int_{-\infty}^{x} [\exp(t)/t]\, dt$ is the exponential integral [*Abramowitz and Stegun*, 1964] and a for room temperature (293 K) is defined as $a = (a^*/293) \times 10^{-10} = 5.53 \times 10^{-10}$ m.

Sample calculations show that the average velocities for constant (equation (9)) and variable viscosity (equation (11)) become indistinguishable for liquid films greater than about 10 nm. We therefore use the simpler expression in (9) for flow in films thicker than 10 nm and the more complex (11) for flow in very thin films.

2.4. Liquid Flow in Corners Bounded by a Vapor Phase

Mathematical expressions for average liquid velocity in corners bounded by liquid-vapor interfaces were derived by *Ransohoff and Radke* [1988]. They used a detailed numerical scheme to solve the Navier-Stokes equations for the assumed geometry and boundary conditions. Their results were reduced to the following general form:

$$\bar{v} = \frac{r(\mu)^2}{\varepsilon\eta_0}\left(-\frac{dP}{dz}\right), \tag{12}$$

where ε is a dimensionless flow resistance parameter dependent on the corner angle γ [*Ransohoff and Radke*, 1988]. The tabulated values of *Ransohoff and Radke* [1988] for ε for different corner angles and for zero surface shear stress (i.e., liquid-vapor interface) were fitted with the following parametric expression (Figure 3):

$$\varepsilon(\gamma) = \exp\left(\frac{b + d\gamma}{1 + c\gamma}\right), \tag{13}$$

with $b = 2.124$, $c = -0.00415$, and $d = 0.00783$ ($r^2 = 0.995$) for γ values in the range of $10° < \gamma < 150°$ (Figure 3).

2.5. Unsaturated Hydraulic Conductivity for Films and Corners

Analogy between average velocity calculated from the Navier-Stokes solutions (equations (9), (11), and (12)) and Darcy's law representation of the liquid flux was used to obtain the hydraulic conductivity for films and corners. Darcy's law is given as

$$\bar{v} = \frac{Q}{A} = \frac{K}{\rho g}\left(-\frac{dP}{dz}\right), \tag{14}$$

where Q is the volumetric discharge rate, A is the cross-sectional area occupied by the liquid, K is the hydraulic conductivity, and g is the acceleration of gravity. Assuming a unit hydraulic gradient, rearranging (14), and inserting the solution in (9), (11), and (12) yield the following expressions for $K(\mu)$:

Flow in films with constant liquid viscosity

$$K_F(\mu) = \frac{\rho g}{3\eta_0} h^2(\mu), \tag{15}$$

Flow in films with variable liquid viscosity

$$K_F(\mu) = \frac{\rho g}{3\eta_0}\frac{B(\mu)}{4h(\mu)}, \tag{16}$$

Corner flow [*Ransohoff and Radke*, 1988]

$$K_C(\mu) = \frac{\rho g}{3\eta_0}\frac{3r^2(\mu)}{\varepsilon}. \tag{17}$$

First, we note that in the derivation of (15)–(17), we implicitly assume vertical fracture surfaces. The results may be extended to tilted fracture surfaces by simply multiplying the terms on the right-hand side of (15)–(17) by the cosine of the tilt angle. Second, effects of gravity on the shape of liquid vapor interfaces are neglected. Third, the definition of unsaturated hydraulic conductivity in the derivations above (and subsequently) is slightly different than the commonly accepted definition requiring knowledge of a cross-sectional area of the porous medium. For known fracture aperture size and average spacing between adjacent fractures these two definitions could be reconciled by redefinition of A in (14). For lack of a better term, for simplicity, and to maintain the usual form of Darcy's law, we use "surface hydraulic conductivity" to describe and characterize the inverse of "surface hydraulic resistivity."

2.6. Hydraulic Conductivity of an Individual Surface Roughness Element

Two averaging methods are applied to derive the effective, unsaturated, hydraulic conductivity for fracture surface roughness elements from their respective film (equations (15) and (16)) and corner (equation (17)) conductivities. One method involves averaging over liquid cross-sectional area in the films and occupying the corner. The other approach averages over the projected lengths of film and partially filled corner segments transverse to flow direction as depicted in Figure 1. The latter method appears advantageous from a practical point of view because quantities can be measured directly. In other words, experimental information on the average hydraulic conductivity per fracture length (transverse to flow) is likely to be more observable than total liquid cross-sectional area. However, for the sake of completeness and to facilitate comparisons, both methods will be developed and discussed.

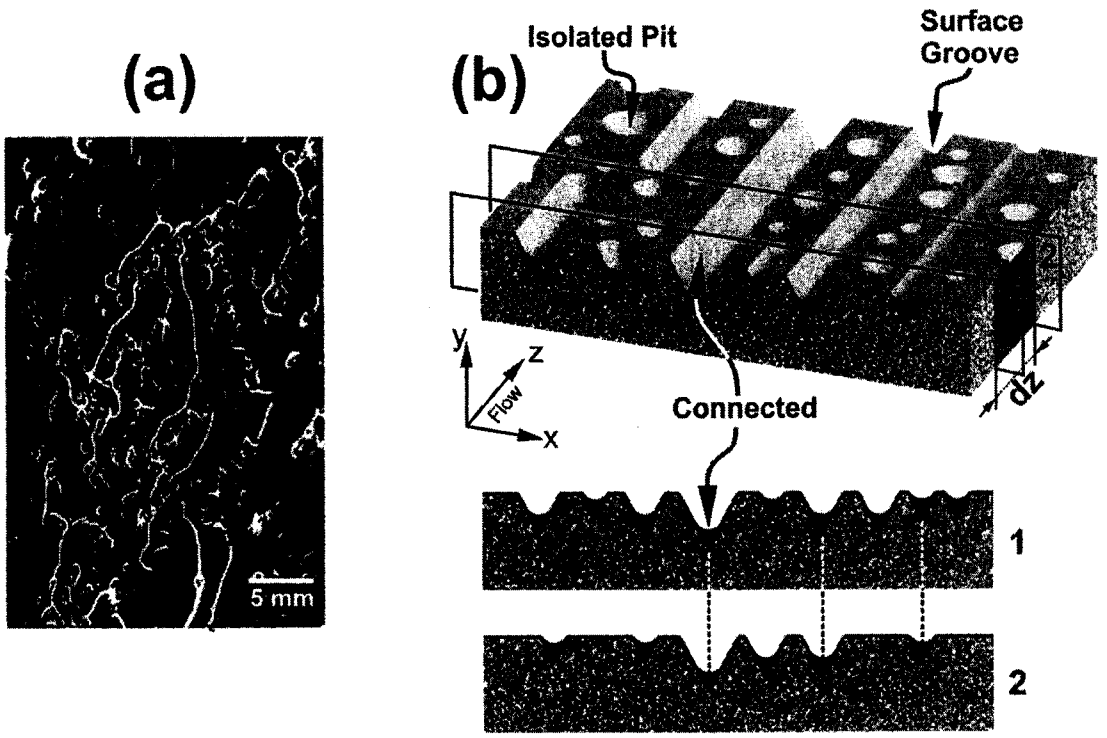

Figure 4. (a) Wet fracture surface of Apache Leap Tuff (Arizona) with visible surface grooves and isolated areas. (b) Geometrical idealization of a rough fracture surface formed by a distribution of roughness elements and illustration of pit/groove connectivity between two adjacent cross sections transverse to flow direction.

2.6.1. Liquid area averaged hydraulic conductivity: $K_A(\mu)$. To obtain expressions for individual roughness element liquid area averaged hydraulic conductivity as a function of matric potential, we must distinguish between two stages of pit filling (completely full and partially filled pits). These two states are separated by the critical matric potential μ_c (equation (6)). The average hydraulic conductivity for matric potentials, which are more negative than the critical matric potential ($\mu < \mu_c$, where pits are partially filled), is given as

$$K_{A1}(\mu) = \frac{K_F(\mu)A_{F1}(\mu) + K_C(\mu)A_{C1}(\mu)\delta}{A_{F1}(\mu) + A_{C1}(\mu)}, \tag{18}$$

where A_{F1} and A_{C1} are the liquid-filled cross-sectional areas of the film and the corner/pit (prior to pit filling), respectively, and δ is a connectivity factor ($0.0 < \delta < 1.0$). The factor δ accounts for partial connectivity among neighboring pits or grooves in the direction of flow (i.e., the fraction of pits and grooves in the cross section that participates in corner flow). When observing adjacent cross sections, not all pits on the fracture wall are likely to be connected to form continuous grooves (see Figure 4). These "isolated" pits are not contributing to corner flow and thus are not considered as part of the K_C contribution (see equation (18)). This spatial connectivity factor is required even at the individual roughness element level for (1) proper introduction of connectivity issues operating at the fracture surface scale and (2) facilitating the use of a single roughness element for representation of the entire fracture surface roughness behavior. For clarity, we show the individual contributions of film $K_{AF1}(\mu)$ and corner flows $K_{AC1}(\mu)$ from (18):

$$K_{AF1}(\mu) = \frac{K_F(\mu)A_{F1}(\mu)}{A_{F1}(\mu) + A_{C1}(\mu)}$$
$$K_{AC1}(\mu) = \frac{K_C(\mu)A_{C1}(\mu)\delta}{A_{F1}(\mu) + A_{C1}(\mu)}. \tag{19}$$

For matric potentials greater than or equal to μ_c, the liquid area averaged hydraulic conductivity is given as

$$K_{A2}(\mu) = \frac{K_F(\mu)A_{F2}(\mu) + K_C(\mu)A_{C2}\delta}{A_{F2}(\mu) + A_{C2}}, \tag{20}$$

where $A_{F2}(\mu)$ and A_{C2} are the liquid-filled cross-sectional areas after a complete filling of the pit. Detailed derivations of $A_{F1}(\mu), A_{C1}(\mu), A_{F2}(\mu)$, and A_{C2} are given in Appendix A. The individual contributions of film and corner flows for this case are derived in the same fashion as for partially filled pits (equation (19)).

2.6.2. Length-averaged hydraulic conductivity: $K_L(\mu)$. Expressions for averaging hydraulic conductivity by the roughness element's projected length transverse to flow are derived in the same fashion considering two pit-filling stages. The fracture length-averaged hydraulic conductivity as a function of matric potential prior to pit filling is given as

$$K_{L1}(\mu) = \frac{K_F(\mu)L_{F1}(\mu) + K_C(\mu)L_{C1}(\mu)}{L_{F1}(\mu) + L_{C1}(\mu)}, \tag{21}$$

and the average hydraulic conductivity after pit filling is defined as

$$K_{L2}(\mu) = \frac{K_F(\mu)L_{F2} + K_C(\mu)L_{C2}}{L_{F2} + L_{C2}}, \tag{22}$$

with $L_{F1}(\mu)$, $L_{C1}(\mu)$, L_{F2}, and L_{C2} as the projected lengths derived in Appendix A.

2.7. Surface Hydraulic Conductivity for an Assemblage of Roughness Elements

A more realistic representation of natural fracture surfaces requires a distribution of roughness element geometric attributes (pit sizes, angles, and associated "flat" segments). A conceptual sketch for a distribution of surface roughness elements on a fracture surface is depicted in Figure 4.

2.7.1. Statistical distribution of pit/groove depths. Fracture surface roughness is represented by a statistical gamma distribution of pit depths (L). The pit angle (γ) is kept constant in subsequent derivations to retain mathematical tractability. The gamma distribution [*Rice*, 1995] facilitates derivation of closed-form expressions for the expected value of fracture surface unsaturated hydraulic conductivity. The gamma density function for the pit depth, $f(L)$, is dependent on two parameters ξ and ω:

$$f(L) = \frac{L^{\xi}}{\xi!\,\omega^{\xi+1}} \exp\left(-\frac{L}{\omega}\right) \qquad L \geq 0. \tag{23}$$

The parameter ξ is limited to integer values only, and $\xi = 2$ was used in this study (to obtain simple and closed-form expressions). The cumulative gamma distribution is expressed as

$$F(L) = \int_0^L \frac{t^2}{2\omega^3} \exp\left(-\frac{t}{\omega}\right) dt \qquad t \geq 0. \tag{24}$$

The range of admissible L values for the assumed gamma distribution was limited to values between $L_{\min}$ and $L_{\max}$, representing the smallest and largest pit depths, respectively. To ensure that the integration of (23) within the limits $L_{\min}$ and $L_{\max}$ is as close to unity as possible or to truncate the distribution tail effect at $L_{\max}$, we minimize the expression

$$\min\left(\int_{L_{\min}}^{L_{\max}} f(L)\, dL - 1\right)$$

(i.e., the deviation between the cumulative gamma distribution and unity) by adjusting ω for a given $L_{\max}$.

2.7.2. Expected value of unsaturated surface hydraulic conductivity. Analogous to hydraulic conductivity calculations for individual elements, we use two different averaging methods, projected length average and liquid cross-sectional area average, to determine unsaturated hydraulic conductivity for an assemblage of elements. In the following we focus on developing expressions for length-averaged hydraulic conductivity because of the more realistic application to observable quantities (see section 2.6).

The average hydraulic conductivity K_L is related to the projected lengths of film and corner flow regions as shown in Figure 1. Closed-form expressions for projected length conductivity K_L as a function of matric potential μ are derived considering two filling stages: partially liquid-filled pits and completely filled pits.

Pits are considered completely full when the curved liquid-vapor interface reaches the pit edge (contact point with the flat segment). The critical pit depth L_1 separating full and partially filled pits varies with the matric potential μ and is calculated from the radius of liquid-vapor interface curvature $r(\mu)$ and pit depth L by rearranging (6):

$$L_1(\mu) = -\frac{\sigma \cos(\gamma/2)}{\rho\mu \tan(\gamma/2)}. \tag{25}$$

The expected value of averaged surface hydraulic conductivity as a function of matric potential $\langle K_L(\mu)\rangle$ is thus expressed as the sum of two terms related to the pit-filling stages:

$$\langle K_L(\mu)\rangle = \langle K_{L1}(\mu)\rangle + \langle K_{L2}(\mu)\rangle, \tag{26a}$$

with

$$\langle K_{L1}(\mu)\rangle = \int_{L_1(\mu)}^{L_{\max}} \frac{K_F(\mu)L_{F1}(\mu) + K_C(\mu)L_{C1}(\mu)}{L_{F1}(\mu) + L_{C1}(\mu)} f(L)\, dL, \tag{26b}$$

$$\langle K_{L2}(\mu)\rangle = \int_{L_{\min}}^{L_1(\mu)} \frac{K_F(\mu)L_{F2} + K_C(\mu)L_{C2}}{L_{F2} + L_{C2}} f(L)\, dL. \tag{26c}$$

The first term (equation (26b)) is the expected value of surface conductivity for partially filled pits obtained by integrating from $L_1(\mu)$ (equation (25)) to the maximum pit depth $L_{\max}$. Equations (15), (16), and (17) are used to calculate corner and film conductivities. The second term $K_{L2}(\mu)$ considers all full pits/grooves. The lower limit of integration is the smallest pit depth $L_{\min}$, set to an arbitrary value of 10 μm in this study, and the upper integration limit is calculated according to (25). To observe the limiting condition for pit filling (when the radius of curvature used in the estimation of K_C (equation (17)) touches pit edge), we relate the curvature to pit geometry by solving (25) for $r(\mu)$ ($r = -\sigma/\rho\mu$) and substitute the resulting expression into (17). The resulting equation for corner hydraulic conductivity $K_C(\mu)$ for full pits is given as

$$K_C(\mu) = L^2 \frac{\tan^2(\gamma/2)\rho g}{\cos^2(\gamma/2)\varepsilon\eta_0}. \tag{27}$$

The film conductivity $K_F(\mu)$ is independent of fracture geometry and is calculated according to (15) and (16), taking into consideration variable liquid viscosity for films thinner than 10 nm. The projected lengths $L_{F1}(\mu)$, $L_{C1}(\mu)$, L_{F2}, and L_{C2} are defined in Appendix A. Detailed solutions for the integrals in (26) are given in Appendix B.

Analytical expressions for the expected value of liquid area averaged hydraulic conductivity $\langle K_A(\mu)\rangle$ are derived in the same fashion as for length-averaged conductivity and are subjected to identical limits of integration:

$$\langle K_A(\mu)\rangle = \langle K_{A1}(\mu)\rangle + \langle K_{A2}(\mu)\rangle, \tag{28a}$$

with

$$\langle K_{A1}(\mu)\rangle = \int_{L_1(\mu)}^{L_{\max}} \frac{K_F(\mu)A_{F1}(\mu) + K_C(\mu)A_{C1}(\mu)\delta}{A_{F1}(\mu) + A_{C1}(\mu)} f(L)\, dL, \tag{28b}$$

$$\langle K_{A2}(\mu)\rangle = \int_{L_{\min}}^{L_1(\mu)} \frac{K_F(\mu)A_{F2}(\mu) + K_C(\mu)A_{C2}\delta}{A_{F2}(\mu) + A_{C2}} f(L)\, dL. \tag{28c}$$

Detailed derivations and closed-form solutions for the integrals are given in Appendix B.

3. Illustrative Examples

We proceed with illustrative examples first for an individual surface roughness element, and then we discuss an ensemble of elements forming rough fracture surfaces. Both the projected surface length (transverse to flow) and the liquid-area-averaging methods are presented. We consider the effects of different groove angles (γ), spacing (βL), and connectivity factors (δ) on calculated surface hydraulic conductivity. These model calculations are compared with experimental results reported by *Tokunaga and Wan* [1997]. All physical constants used in the calculations are listed in Table 1.

3.1. Hydraulic Conductivity of a Representative Surface Roughness Element

The modeling approach was tested using a unique data set obtained by *Tokunaga and Wan* [1997] from flow measurements on a Bishop tuff sample. Liquid retention on the rock surface as a function of matric potential was calculated and compared with experimental results expressed as a uniform "effective" film thickness. Representative geometrical parameters (L, β, δ, and γ) were adjusted to yield the best match between model calculations and measurements (Figure 5a). The modeled "effective" film thickness as a function of μ was calculated by dividing the liquid-filled cross-sectional area by the projected roughness element length ($\beta L + 2L \tan(\gamma/2)$, see Figure 1). The potential range of L was constrained to observed values reported by *Tokunaga and Wan* [1997] where most of the variations in surface "elevation" were between 0.5 and 2 mm. The individual contributions of capillarity and adsorption to liquid storage are illustrated and show a crossover for matric potential values of $\mu = -1$ to -2 J kg^{-1} (very wet conditions). These values of matric potential represent a rough demarcation between fast corner and slow film flows.

Fracture length-averaged unsaturated hydraulic conductivity $K_L(\mu)$ (equation (26)) was calculated for the same element geometry as used for "effective film" calculations (i.e., $L = 10^{-3}$ m, $\beta = 4$, and $\gamma = 120°$). The average film velocity reported by *Tokunaga and Wan* [1997, Figure 8] was obtained by two methods: (1) using the average film thickness in the smooth film (equation (15), denoted as v-bar) and (2) dividing the estimated transmissivity by the effective film thickness (denoted as T). The connectivity factor δ is an additional parameter required for matching calculated and experimental surface hydraulic conductivity. The results with $\delta = 0.1$ are depicted in Figure 5b showing a reasonable agreement between calculated $K_L(\mu)$ and *Tokunaga and Wan*'s [1997] average film velocities that were measured under unit hydraulic gradient conditions.

Table 1. Physical Constants and Dimensions Used in the Illustrative Example Calculations

Property	Symbol	Value	Unit
Acceleration of gravity	g	9.81	m s^{-2}
Density of water, 20°C	ρ	998	kg m^{-3}
Hamaker constant (solid-vapor through intervening liquid)	A_{svl}	−1.9E-19	J
Surface tension water-vapor interface, 20°C	σ	0.07275	N m^{-1}
Viscosity constant	a	5.53E-10	m
Viscosity of water, 20°C	η_0	0.001002	kg m^{-1} s^{-1}

Read −1.9E-19 as -1.9×10^{-19}.

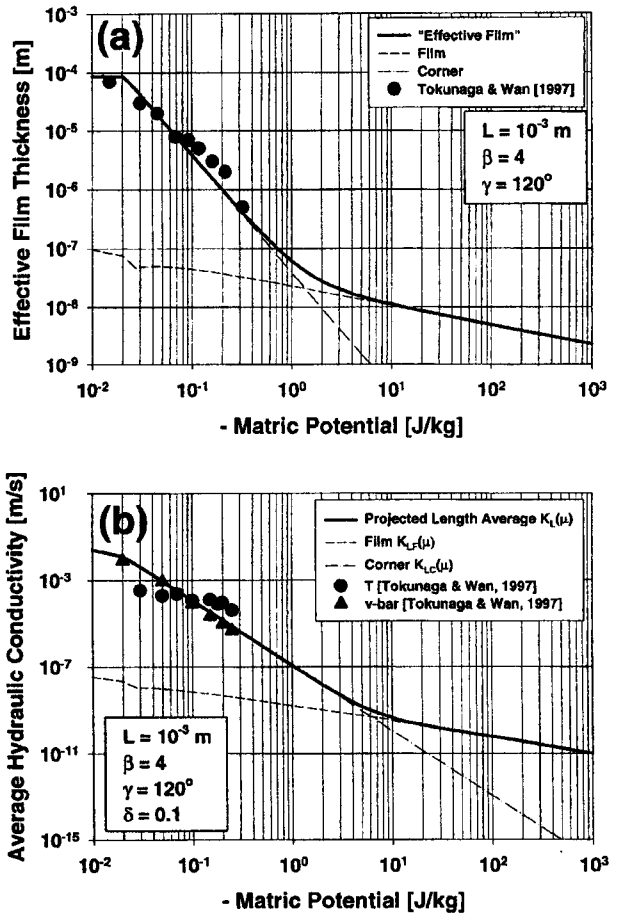

Figure 5. Comparison of model calculations for an individual fracture element with experimental data of *Tokunaga and Wan* [1997]: (a) effective film thickness and (b) average hydraulic conductivity with T denoting transmissivity divided by the average film thickness; v-bar denotes average film velocity evaluated with the smooth film equation [*Tokunaga and Wan*, 1997].

The contributions of corners (K_{LC}) and films (K_{LF}) to the overall value of $K_L(\mu)$ are shown. Similar to liquid storage behavior, a crossover from corner domination to film domination is observed near matric potential values of $\mu < -6$ J kg^{-1}. The simultaneous agreement with average film thickness and film velocity (which for a unit gradient equals surface conductivity) is remarkable considering the use of only one surface roughness element for both processes. These results illustrate the potential usefulness of the proposed approach for modeling liquid retention and conductivity on rough rock surfaces.

We investigated effects of surface roughness on liquid storage and surface hydraulic conductivity for $\delta = 1.0$ (100% connectivity) by comparing two different groove densities characterized by the spacing parameter β. The results for a surface represented by an individual element are depicted in Figure 6a for $\beta = 1$ (small spacing equals rough surface) and are depicted in Figure 6b for $\beta = 100$ (large spacing equals smooth surface). As expected, surface liquid retention (expressed as effective film thickness) for a given matric potential was larger for the rough surface relative to the smooth surface. The storage difference diminishes with decreasing matric potential

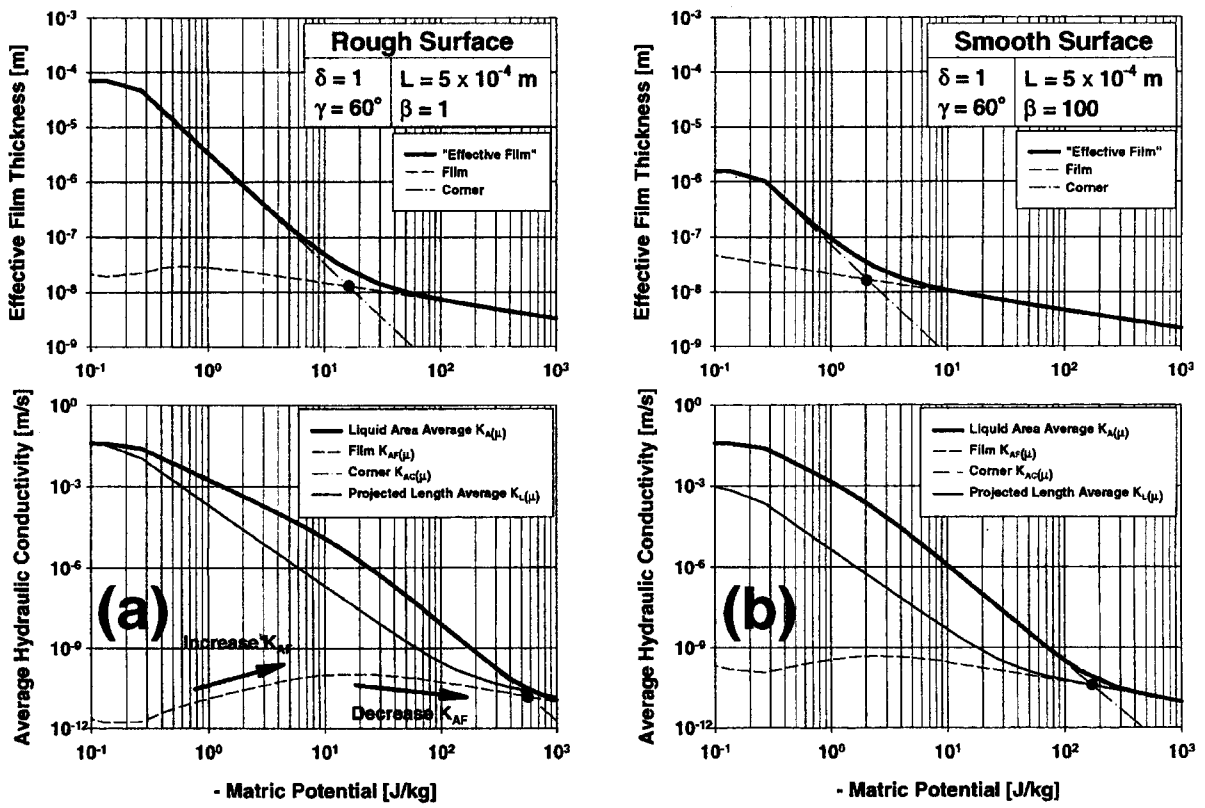

Figure 6. Model calculations of individual element's effective film thickness and unsaturated hydraulic conductivity for (a) small β (rough surface) and (b) high β (smooth surface). Note the increase in film contribution to hydraulic conductivity.

(more negative), and the amount of liquid storage for $\mu < -100$ J kg^{-1} is very similar (dominated by thin liquid films). The crossover between capillary- and film-dominated storage occurs at lower potential values for the rough surface.

Significant differences were found in the behavior of $K_L(\mu)$ and $K_A(\mu)$, especially for the smooth surface (Figure 6b, bottom). The $K_L(\mu)$ value for a rough surface is approximately in the same range as that of $K_A(\mu)$ at high potentials, whereas for smooth surfaces a difference of about 2 orders of magnitude exists $[K_A(\mu) > K_L(\mu)]$. These differences diminish with decreasing matric potential (as it becomes more negative) until they practically vanish when film flow becomes dominant. These differences are attributed to the large carrying capacity of corner flow over a similar liquid cross section in a film configuration. The transition from corner- to film-dominated flow regimes for a smooth surface occurs at higher potentials than for the rough surface (similar to the liquid storage behavior).

An interesting transitional behavior in film contribution (K_{AF}) to $K_A(\mu)$ as a function of μ is observed for the two surfaces (more pronounced in the rough surface). The increase and later a decrease in film contribution represent an interplay between the reduction of film thickness with decreasing potential and the creation of new film surfaces with the receding menisci into the grooves and pits. The total response is dependent on the proportions of these two opposing processes as shown in Figure 6.

3.2. Hydraulic Conductivity of Rough Fracture Surfaces: Statistical Considerations

The statistical representation of pit depth (L) yields analytical expressions for the expected values of "effective" film thickness, liquid-area-averaged hydraulic conductivity $\langle K_A(\mu)\rangle$ (where angle brackets denote the expected value operation), and fracture length-weighted unsaturated hydraulic conductivity $\langle K_L(\mu)\rangle$. To test the analytical solutions, we again used the experimental data of *Tokunaga and Wan* [1997] in the same fashion as for the representative (individual) roughness element. The maximum pit depth for the gamma-distributed L was set to 3 mm, and the pit angle was fixed at 120°. The other parameters that provided the best fit to the data were $\beta = 8$ and $\delta = 0.1$. Surprisingly, there was little difference in model performance between the individual representative element and the statistical representation using a population of roughness elements (Figure 7). The only difference was smoother transitions in the hydraulic conductivity curve (and slightly different fitting parameters). The results of this limited test reinforce our conclusion that a representative surface roughness element is capable of modeling effective film thickness and unsaturated conductivity of rough fracture surfaces.

The relationships between surface length-weighted hydraulic conductivity, $\langle K_L(\mu)\rangle$, and liquid-area-averaged hydraulic conductivity $\langle K_A(\mu)\rangle$ for two different pit angles ($\gamma = 30°$ and 120°) are depicted in Figure 8. Liquid-area-averaged hydraulic

conductivity $\langle K_A(\mu)\rangle$ was higher than the projected length-averaged conductivity $\langle K_L(\mu)\rangle$ (for the assumed geometry) over the entire range of matric potentials considered ($-0.001 < \mu < -400{,}000$ J kg^{-1}). While calculations for $\gamma = 30°$ are reasonably close to the 1:1 line, large differences at midrange of matric potential values are observed for $\gamma = 120°$. These differences may be attributed to the relatively large carrying capacity of corner flow for $\gamma = 120°$ that tends to be underestimated by the length-averaging procedure. Note that the cross-sectional area of grooves with a larger angle ($\gamma = 120°$) tend to be larger than that for a smaller angle ($\gamma = 30°$).

4. Summary and Conclusions

A simple geometrical model for rough fracture surfaces was proposed to provide a tractable geometry for calculations of surface liquid retention due to adsorbed films and capillary liquid. Assuming slow laminar flow and stable liquid configurations, the average hydraulic conductivity for film and corner flows was derived. Coupled with information on the relative fracture area under each flow regime, the proposed model led to calculation of unsaturated hydraulic conductivity for a representative element (including connectivity factor) and an ensemble of gamma-distributed surface roughness elements. The calculated values of surface storage and hydraulic conductivity with geometrical parameter fitting resulted in excellent agreement with the experimental data of *Tokunaga and Wan* [1997]. Similar results were obtained for the statistical representation of roughness elements and the same experimental data. These findings illustrate the usefulness of the proposed roughness geometry where a single representative roughness element was sufficient to explain both surface storage and unsaturated hydraulic conductivity data of *Tokunaga and Wan* [1997].

An interesting transitional behavior in film contribution (K_{AF}) to the overall hydraulic conductivity can be observed, showing an increase and later a decrease in film flow contribution with decreasing matric potential. This response represents interplay between the reduction of film thickness with decreasing potential and the creation of new film surfaces with the receding menisci into grooves and pits. It is clear from model calculations and experimental evidence that film contribution to unsaturated flow is not negligible as argued by some earlier studies [*Dullien et al.*, 1986]; it becomes a dominating mechanism for relatively wet conditions on the order of $\mu < -5$ J kg^{-1}.

One of the primary advantages of the proposed model is the direct link with rock matrix processes through the system's matric potential. However, this is limited (at this stage) to equilibrium liquid configurations, because dynamic exchange processes between the two flow systems are not considered. The unsaturated hydraulic conductivity of rough fracture surfaces represents a first step toward development of a comprehensive model for liquid retention and hydraulic conductivity of unsaturated fractured porous media using a similar modeling approach and a distribution of fracture apertures. Liquid behavior near asperities and in contact points between two fracture surfaces is not addressed in this study. These important geometrical features found in many fractured systems will be a subject of future analyses of fractured porous media using

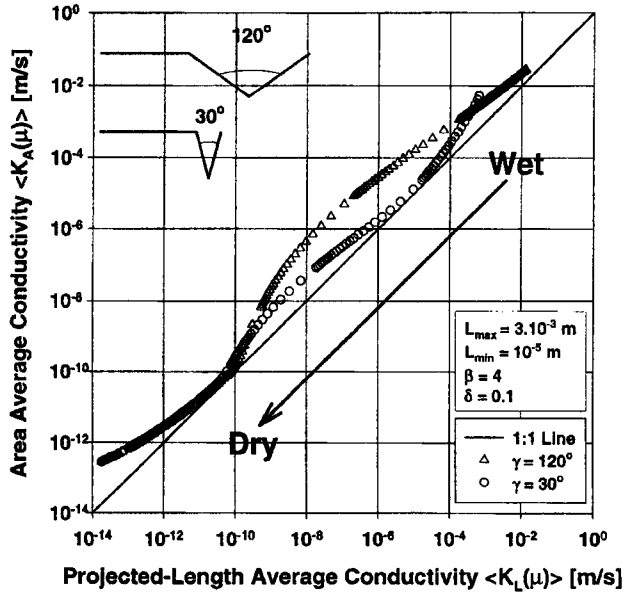

Figure 8. The relationships between the expected values (statistical representation) of unsaturated hydraulic conductivity for liquid cross-sectional area average $\langle K_A\rangle$ versus fracture length average $\langle K_L\rangle$ for groove angles of 30° and 120°.

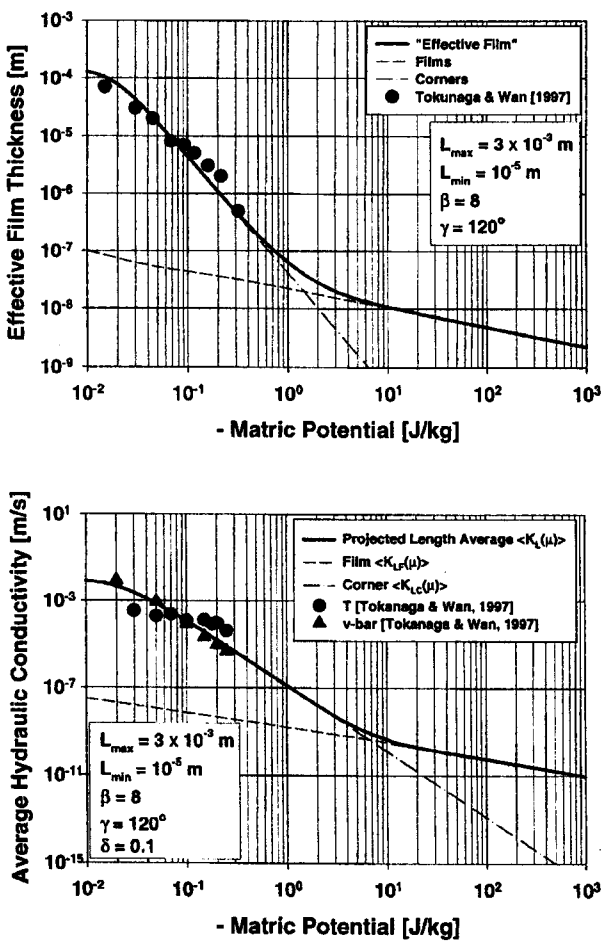

Figure 7. Comparison of model calculations for a statistical distribution of surface roughness elements with experimental data of *Tokunaga and Wan* [1997]: (a) effective film thickness and (b) average hydraulic conductivity.

derivations for liquid configuration presented by *Tuller et al.* [1999].

Appendix A: Solutions for a Single Roughness Element

In the following we derive the expressions for film- and corner-associated liquid-filled cross-sectional areas and projected lengths used in sections 2.6.1 and 2.6.2 to calculate average fracture element conductivities prior and after to pit filling.

A1. Liquid-Filled Cross-Sectional Areas Prior to Pit Filling ($\mu < \mu_c$)

The derivations for liquid-filled cross-sectional areas prior to pit filling were principally already introduced in section 2.2. The liquid-filled cross-sectional area in corners $A_{C1}(\mu)$ is calculated according to (3), and the film area $A_{F1}(\mu)$ is calculated according to (5).

A2. Liquid-Filled Cross-Sectional Areas After Pit Filling ($\mu \geq \mu_c$)

The cross-sectional area of liquid retained in the corner is given as

$$A_{C2} = L^2 \tan(\gamma/2). \tag{A1}$$

The cross-sectional area of the liquid film is defined as

$$A_{F2}(\mu) = h(\mu)[L\beta + 2(1-\delta)L \tan(\gamma/2)]. \tag{A2}$$

It seems reasonable to ignore the contribution of the film forming over a flowing groove area because of surface perturbations introduced by the hydrodynamic regime within the groove below. The situation must be rectified for nonflowing pits where local depressions in the liquid-vapor interface (after pit filling) are not likely to be sustainable (from surface energy considerations). Thus we propose to base the correction on the fraction of connected and flowing pits $(1-\delta)$, where δ is a "pit connectivity" factor.

A3. Calculating the Projected Lengths Prior to Pit Filling ($\mu < \mu_c$)

The average surface conductivity $K_L(\mu)$ (equations (21) and (22)) is related to the projected lengths (transverse to flow direction) of the regions with film and corner flow as shown in Figure 1. The projected length of film- and corner-covered surface area prior to pit filling is given as

$$L_{F1}(\mu) = L[\beta + 2\tan(\gamma/2)] - 2\delta r(\mu)\cos(\gamma/2), \tag{A3}$$

$$L_{C1}(\mu) = 2\delta r(\mu)\cos(\gamma/2). \tag{A4}$$

A4. Calculating the Projected Lengths after Pit Filling ($\mu \geq \mu_c$)

The projected lengths after pit filling are defined as

$$L_{F2} = L[\beta + 2(1-\delta)\tan(\gamma/2)], \tag{A5}$$

$$L_{C2} = 2L\delta \tan(\gamma/2). \tag{A6}$$

Appendix B: Analytical Solutions for a Population of Roughness Elements

In the following we outline detailed solutions for the projected lengths and liquid cross-section-averaged hydraulic conductivities of a fracture surface.

B1. Projected Length-Averaged Hydraulic Conductivity

The solution for fracture elements with partially filled pits (equation (26b)) is given as

$$\begin{aligned}\langle K_{L1}(\mu)\rangle = \frac{1}{2(2C_1+\beta)\omega^2}[&V_1(\mu)(V_2(\mu)(K_C(\mu)-K_F(\mu))\\ &\cdot(L_1(\mu)+\omega) + K_F(\mu)(2C_1+\beta)(L_1(\mu)^2\\ &+ 2L_1(\mu)\omega + 2\omega^2))\\ &- C_2(V_2(\mu)(K_C(\mu)-K_F(\mu))\\ &\cdot(L_{\max}+\omega) + K_F(\mu)(2C_1+\beta)\\ &\cdot(L_{\max}^2 + 2L_{\max}\omega + 2\omega^2))],\end{aligned} \tag{B1}$$

with the constants

$$C_1 = \tan(\gamma/2),$$

$$C_2 = \exp\left(-\frac{L_{\max}}{\omega}\right)$$

and the variables

$$V_1(\mu) = \exp\left(-\frac{L_1(\mu)}{\omega}\right),$$

$$V_2(\mu) = 2\delta r(\mu)\cos(\gamma/2).$$

The contribution of the films in fracture elements with partially filled pits is calculated as

$$\begin{aligned}\langle K_{L1F}(\mu)\rangle = \frac{K_F(\mu)}{2(2C_1+\beta)\omega^2}\{&V_1(\mu)[-V_2(\mu)(L_1(\mu)+\omega)\\ &+ (2C_1+\beta)(L_1(\mu)^2 + 2L_1(\mu)\omega + 2\omega^2)]\\ &- C_2[-V_2(\mu)(L_{\max}+\omega) + (2C_1+\beta)\\ &\cdot(L_{\max}^2 + 2L_{\max}\omega + 2\omega^2)]\}.\end{aligned} \tag{B2}$$

The contribution of corners is given as

$$\begin{aligned}\langle K_{L1C}(\mu)\rangle = &\frac{V_2(\mu)K_C(\mu)}{2(2C_1+\beta)\omega^2}\\ &\cdot[V_1(\mu)(L_1(\mu)+\omega) - C_2(L_{\max}+\omega)].\end{aligned} \tag{B3}$$

The solution for the second term (equation (26c)) is given as

$$\begin{aligned}\langle K_{L2}(\mu)\rangle = [2(C_4+C_5)\omega^2]^{-1}\{&-V_1(\mu)[C_4K_F(\mu)\\ &\cdot(L_1(\mu)^2 + 2L_1(\mu)\omega + 2\omega^2) + C_3C_5(L_1(\mu)^4\\ &+ 4L_1(\mu)^3\omega + 12L_1(\mu)^2\omega^2 + 24L_1\omega^3 + 24\omega^4)]\\ &+ C_6[C_4K_F(\mu)(L_{\min}^2 + 2L_{\min}\omega + 2\omega^2)\\ &+ C_3C_5(L_{\min}^4 + 4L_{\min}^3\omega + 12L_{\min}^2\omega^2\\ &+ 24L_{\min}\omega^3 + 24\omega^4)]\},\end{aligned} \tag{B4}$$

with the constants

$$C_3 = \frac{C_1^2\rho g}{\cos^2(\gamma/2)\varepsilon\eta_0},$$

$$C_4 = \beta + 2(1-\delta)C_1,$$

$$C_5 = 2\delta C_1,$$

$$C_6 = \exp\left(-\frac{L_{\min}}{\omega}\right).$$

The contribution of the films in fracture elements with full pits is calculated as

$$\langle K_{L2F}(\mu)\rangle = \frac{C_4 K_F(\mu)}{2(C_4 + C_5)\omega^2}[-V_1(\mu)(L_1(\mu)^2 + 2L_1(\mu)\omega + 2\omega^2) + C_6(L_{\min}^2 + 2L_{\min}\omega + 2\omega^2)]. \quad \text{(B5)}$$

The contribution of corners is given as

$$\langle K_{L2C}(\mu)\rangle = \frac{C_3 C_5}{2(C_4 + C_5)\omega^2}[-V_1(\mu)(L_1(\mu)^4 + 4L_1(\mu)^3\omega + 12L_1(\mu)^2\omega^2 + 24L_1(\mu)\omega^3 + 24\omega^4) + C_6(L_{\min}^4 + 4L_{\min}^3\omega + 12L_{\min}^2\omega^2 + 24L_{\min}\omega^3 + 24\omega^4)]. \quad \text{(B6)}$$

B2. Liquid Cross-Section-Averaged Hydraulic Conductivity

Closed-form expressions for liquid cross-sectional area averaged hydraulic conductivity are somewhat more complicated involving exponential integrals. The analytical solution for (28b) is given as

$$\begin{aligned}\langle K_{A1}\rangle = \frac{1}{2V_3(\mu)^2\omega^2}\{&V_1(\mu)[V_4(\mu)(V_5(\mu)\delta K_C(\mu) - V_5(\mu)K_F(\mu)) \\ &+ V_5(\mu)\delta K_C(\mu)[-V_5(\mu) + V_3(\mu)(L_1(\mu) + \omega)] \\ &+ K_F(\mu)[V_5(\mu)^2 - V_3(\mu)V_5(\mu)(L_1(\mu) + \omega) \\ &+ V_3(\mu)^2(L_1(\mu)^2 + 2L_1(\mu)\omega + 2\omega^2)]] \\ &- C_6(V_4(\mu)(V_5(\mu)\delta K_C(\mu) - V_5(\mu)K_F(\mu)) \\ &+ V_5(\mu)\delta K_C(\mu)[-V_5(\mu) + V_3(\mu)(L_{\max} + \omega)] \\ &+ K_F(\mu)[V_5(\mu)^2 - V_3(\mu)V_5(\mu)(L_{\max} + \omega) \\ &+ V_3(\mu)^2(L_{\max}^2 + 2L_{\max}\omega + 2\omega^2)]]\} \\ &+ \{(V_4(\mu) - V_5(\mu))^2 V_6(\mu)(-V_5(\mu)\delta K_C(\mu) + V_5(\mu)K_F(\mu)) \\ &\cdot(-E_1[U_1(\mu)] + E_1[U_2(\mu)])\}[2V_3(\mu)^3\omega^3]^{-1}, \quad \text{(B7)}\end{aligned}$$

with the variables

$$V_3(\mu) = h(\mu)\left(\beta + \frac{2}{\cos\left(\frac{\gamma}{2}\right)}\right),$$

$$V_4(\mu) = \frac{2h(\mu)r(\mu)}{C_1},$$

$$V_5(\mu) = r(\mu)^2 F,$$

$$V_6(\mu) = \exp\left(\frac{-V_4(\mu) + V_5(\mu)}{V_3(\mu)\omega}\right)$$

and the arguments of the exponential integrals $E_1[U]$

$$U_1(\mu) = \frac{-V_4(\mu) + V_5(\mu) + V_3(\mu)L_1(\mu)}{V_3(\mu)\omega}$$

$$U_2(\mu) = \frac{-V_4(\mu) + V_5(\mu) + V_3(\mu)L_{\max}}{V_3(\mu)\omega}.$$

The exponential integral $E_1[U]$ is defined as

$$E_1[U] = \int_U^\infty [\exp(-t)/t]\, dt$$

and must be evaluated numerically using standard mathematical software (e.g., Mathematica, Wolfram Res., Inc.). For arguments in the range $0 < U \leq 15$ the following series expansion may be applied for the evaluation:

$$E_1[U] = -\gamma^* - \ln[U] - \sum_{n=1}^{150} \frac{(-1)^n U^n}{nn!}.$$

where $\gamma^* = 0.57721566\ldots$ (Euler's constant). The contribution of films is given as

$$\begin{aligned}\langle K_{A1F}\rangle = \frac{K_F(\mu)}{2V_3(\mu)^3\omega^3}\{&V_3(\mu)\omega[C_6[V_4(\mu)V_5(\mu) - V_5(\mu)^2 \\ &+ V_3(\mu)V_5(\mu)L_{\max} - V_3(\mu)^2L_{\max}^2 + V_3(\mu)\omega(V_5(\mu) \\ &- 2V_3(\mu)L_{\max}) - 2V_3(\mu)^2\omega^2] + V_1(\mu)[-V_4(\mu)V_5(\mu) \\ &+ V_5(\mu)^2 - V_3(\mu)V_5(\mu)(L_1(\mu) + \omega) + V_3(\mu)^2(L_1(\mu)^2 \\ &+ 2L_1(\mu)\omega + 2\omega^2)]] + (V_4(\mu) - V_5(\mu))^2V_5(\mu)V_6(\mu) \\ &\cdot(-E_1[U_1(\mu)] + E_1[U_2(\mu)])\} \quad \text{(B8)}\end{aligned}$$

The contribution of corners is given as

$$\begin{aligned}\langle K_{A1C}\rangle = \frac{V_5(\mu)\delta K_C(\mu)}{2V_3(\mu)^3\omega^3}\{&V_3(\mu)\omega[V_1(\mu)[V_4(\mu) - V_5(\mu) \\ &+ V_3(\mu)(L_1(\mu) + \omega)] - C_6[V_4(\mu) - V_5(\mu) + V_3(\mu) \\ &\cdot(L_{\max} + \omega)]] - (V_4(\mu) - V_5(\mu))^2V_6(\mu)(-E_1[U_1(\mu)] \\ &+ E_1[U_2(\mu)])\}. \quad \text{(B9)}\end{aligned}$$

The analytical solution for (28c) representing full pits is given as

$$\begin{aligned}\langle K_{A2}(\mu)\rangle = \frac{1}{2C_1^6\omega^3}\Bigg\{&C_1\omega\Bigg\{-V_1(\mu)\Bigg[C_1^3V_7(\mu)K_F(\mu) \\ &\cdot[-V_7(\mu) + C_1(L_1(\mu) + \omega)] \\ &+ C_2\frac{C_4}{2}[V_7(\mu)^4 - C_1V_7(\mu)^3(L_1(\mu) + \omega) \\ &+ C_1^2V_7(\mu)^2(L_1(\mu)^2 + 2L_1(\mu)\omega + 2\omega^2) - C_1^3V_7(\mu) \\ &\cdot(L_1(\mu)^3 + 3L_1(\mu)^2\omega + 6L_1(\mu)\omega^2 + 6\omega^3) + C_1^4(L_1(\mu)^4 \\ &+ 4L_1(\mu)^3\omega + 12L_1(\mu)^2\omega^2 + 24L_1(\mu)\omega^3 + 24\omega^4)]\Bigg] \\ &+ C_5\Bigg[C_1^3V_7(\mu)K_F(\mu)[-V_7(\mu) + C_1(L_{\min} + \omega)] \\ &+ C_2\frac{C_4}{2}[V_7(\mu)^4 - C_1V_7(\mu)^3(L_{\min} + \omega) \\ &+ C_1^2V_7(\mu)^2(L_{\min}^2 + 2L_{\min}\omega + 2\omega^2) - C_1^3V_7(\mu)(L_{\min}^3 \\ &+ 3L_{\min}^2\omega + 6L_{\min}\omega^2 + 6\omega^3) + C_1^4(L_{\min}^4 + 4L_{\min}^3\omega \\ &+ 12L_{\min}^2\omega^2 + 24L_{\min}\omega^3 + 24\omega^4)]\Bigg]\Bigg\} \\ &- V_7(\mu)^3V_8(\mu)\left(C_2V_7(\mu)^2\frac{C_4}{2} - C_1^3K_F(\mu)\right) \\ &\cdot(-E_1[U_3(\mu)] + E_1[U_4(\mu)])\Bigg\}, \quad \text{(B10)}\end{aligned}$$

with the variables

$$V_7(\mu) = h(\mu)C_3,$$

$$V_8(\mu) = \exp\left(\frac{V_7(\mu)}{C_1\omega}\right)$$

and the arguments of the exponential integrals $E_1[U]$

$$U_3(\mu) = \frac{V_7(\mu) + C_1L_1(\mu)}{C_1\omega},$$

$$U_4(\mu) = \frac{V_7(\mu) + C_1L_{\min}}{C_1\omega}.$$

The contribution of films to (28c) is given as

$$\langle K_{A2F}\rangle = \frac{V_7(\mu)K_F(\mu)}{2C_1^3\omega^3}(C_1V_1(\mu)\omega[V_7(\mu) - C_1(L_1(\mu) + \omega)] + C_1C_5\omega[-V_7(\mu) + C_1(L_{\min} + \omega)] + V_7(\mu)^2V_8(\mu) \cdot (-E_1[U_3(\mu)] + E_1[U_4(\mu)])). \quad \text{(B11)}$$

The corner contribution is given as

$$\langle K_{A2C}\rangle = \frac{C_2C_4}{4C_1^6\omega^3}(C_1\omega(-V_1(\mu)(V_7(\mu)^4 - C_1V_7(\mu)^3(L_1(\mu) + \omega) + C_1^2V_7(\mu)^2(L_1(\mu)^2 + 2L_1(\mu)\omega + 2\omega^2) - C_1^3V_7(\mu)(L_1(\mu)^3 + 3L_1(\mu)^2\omega + 6L_1(\mu)\omega^2 + 6\omega^3) + C_1^4(L_1(\mu)^4 + 4L_1(\mu)^3\omega + 12L_1(\mu)^2\omega^2 + 24L_1(\mu)\omega^3 + 24\omega^4)) + C_5(V_7(\mu)^4 - C_1V_7(\mu)^3(L_{\min} + \omega) + C_1^2V_7(\mu)^2(L_{\min}^2 + 2L_{\min}\omega + 2\omega^2) - C_1^3V_7(\mu)(L_{\min}^3 + 3L_{\min}^2\omega + 6L_{\min}\omega^2 + 6\omega^3) + C_1^4(L_{\min}^4 + 4L_{\min}^3\omega + 12L_{\min}^2\omega^2 + 24L_{\min}\omega^3 + 24\omega^4))) - V_7(\mu)^5V_8(\mu) \cdot (-E_1[U_3(\mu)] + E_1[U_4(\mu)])). \quad \text{(B12)}$$

Notation

- β dimensionless parameter relating pit spacing to pit depth.
- γ pit angle [deg].
- δ dimensionless pit connectivity factor.
- ε dimensionless flow resistance parameter.
- η modified liquid viscosity in vicinity of solid surfaces [kg m^{-1} s^{-1}].
- η_0 liquid viscosity [kg m^{-1} s^{-1}].
- μ matric potential [J kg^{-1}].
- μ_c critical matric potential separating partially filled and full pits [J kg^{-1}].
- ξ gamma distribution parameter.
- ρ density of the liquid [kg m^{-3}].
- σ surface tension at the liquid-vapor interface [N m^{-1}].
- ω gamma distribution parameter.
- a^* constant for modified liquid viscosity in vicinity of solid surfaces [Å K].
- a viscosity constant [m].
- $A_C(\mu)$ liquid-occupied cross-sectional area in a corner [m^2].
- $A_F(\mu)$ liquid-occupied cross-sectional film area [m^2].
- A_{svl} Hamaker constant for solid-vapor interactions through intervening liquid [J].
- $B(\mu)$ thin film variable viscosity function in equation (11).
- E_1 exponential integral [*Abramowitz and Stegun*, 1964].
- $F(L)$ cumulative gamma distribution.
- $f(L)$ gamma density distribution.
- $F(\gamma)$ angularity factor.
- g acceleration of gravity [m s^{-2}].
- $h(\mu)$ film thickness [m].
- $K(\mu)$ unsaturated hydraulic conductivity [m s^{-1}].
- $K_C(\mu)$ mean corner hydraulic conductivity [m s^{-1}].
- $K_F(\mu)$ mean film hydraulic conductivity [m s^{-1}].
- L pit depth [m].
- $L_{\max}$ maximal pit depth [m].
- $L_{\min}$ minimal pit depth [m].
- P hydraulic pressure head [m].
- $r(\mu)$ radius of liquid-vapor interface curvature [m].
- U argument of the exponential integral E_1.
- $\bar{v}$ average liquid velocity [m s^{-1}].
- z spatial coordinate along flow path [m].

Acknowledgments. The authors gratefully acknowledge the partial support of NSF under grant EAR-9805409, the Nuclear Regulatory Commission (NRC) under contract NRC-02-97-009 to the Center for Nuclear Waste Regulatory Analysis (CNWRA), and the Utah Agricultural Experimental Station (UAES). Special thanks go to Teamrat Ghezzehei (USU) for assistance with graphics, to Ron Green (CNWRA) for a thorough review of an earlier version of the manuscript, and to Randy Fedors, Stu Stothoff, and Debra Hughson (CNWRA) for their support and insightful advice. The authors express their gratitude to Tetsu Tokunaga, Todd Rasmussen, and an anonymous reviewer for their insightful comments, leading to substantial improvements of the manuscript. This paper is an independent product of a contract to the CNWRA and does not necessarily reflect the view or regulatory position of the NRC. This is approved as UAES journal paper 7193.

References

Abramowitz, M., and I. E. Stegun (Eds.), *Handbook of Mathematical Functions With Formulas, Graphs, and Mathematical Tables*, *Appl. Math. Ser.*, vol. 55, Natl. Inst. of Stand. and Technol., Gaithersburg, Md., 1964.

Colbeck, S. C., Capillary bonding of wet surfaces, *Surf. Coat. Technol.*, *81*, 209–214, 1996.

Derjaguin, B. V., N. V. Churaev, and V. M. Muller, *Surface Forces*, Consult. Bur., New York, 1987.

Dullien, F. A. L., F. S. Y. Francis, and I. F. MacDonald, Hydraulic continuity of residual wetting phase in porous media, *J. Colloid Interface Sci.*, *109*, 201–218, 1986.

Fischer, U., B. Kulli, and H. Flühler, Constitutive relationships and pore structure of undisturbed fracture zone samples with cohesionless fault gouge layers, *Water Resour. Res.*, *34*(7), 1695–1701, 1998.

Fourar, M., S. Bories, R. Lenormand, and P. Persoff, Two-phase flow in smooth and rough fractures: Measurement and correlation by porous medium and pipe flow models, *Water Resour. Res.*, *29*(11), 3699–3708, 1993.

Glass, R. J., M. J. Nicholl, and V. C. Tidwell, Challenging models for flow in unsaturated, fractured rock through exploration of small-scale processes, *Geophys. Res. Lett.*, *22*, 1457–1460, 1995.

Iwamatsu, M., and K. Horii, Capillary condensation and adhesion of two wetter surfaces, *J. Colloid Interface Sci.*, *182*, 400–406, 1996.

Low, P. F., Viscosity of interlayer water in montmorillonite, *Soil Sci. Soc. Am. J.*, *40*, 500–505, 1976.

Low, P. F., Nature and properties of water in montmorillonite-water systems, *Soil Sci. Soc. Am. J.*, *43*, 651–658, 1979.

McBride, M. B., and P. Baveye, Mobility of anion spin probes in hectorite gels: Viscosity of surficial water, *Soil Sci. Soc. Am. J.*, *59*, 388–394, 1995.

Novy, R. A., P. G. Toledo, H. T. Davis, and L. E. Scriven, Capillary dispersion in porous media at low wetting phase saturations, *Chem. Eng. Sci.*, *44*(9), 1785–1797, 1989.

Or, D., and M. Tuller, Liquid retention and interfacial area in variably saturated porous media: Upscaling from single-pore to sample-scale model, *Water Resour. Res.*, *35*(12), 3591–3606, 1999.

Or, D., and J. M. Wraith, Temperature effects on soil bulk dielectric permittivity measured by time domain reflectometry: A physical model, *Water Resour. Res.*, *35*(2), 371–383, 1999.

Philip, J. R., Adsorption and capillary condensation on rough surfaces, *J. Phys. Chem.*, *82*(12), 1379–1385, 1978.

Pozrikidis, C., The flow of a liquid film along a periodic wall, *J. Fluid Mech.*, *188*, 275–300, 1988.

Pruess, K., A mechanistic model for water seepage through thick unsaturated zones in fractured rocks of low matrix permeability, *Water Resour. Res.*, *35*(4), 1039–1051, 1999.

Pruess, K., and T. N. Narasimhan, On fluid reserves and production of superheated steam from fractured, vapor-dominated geothermal reservoir, *J. Geophys. Res.*, *87*(B11), 9329–9339, 1982.

Ransohoff, T. C., and C. J. Radke, Laminar flow of a wetting liquid along the corners of a predominantly gas-occupied noncircular pore, *J. Colloid Interface Sci.*, *121*, 392–401, 1988.

Rasmussen, T. C., Computer simulation model of steady fluid flow and solute transport through three-dimensional networks of variably saturated, discrete fractures, in *Flow and Transport Through Unsaturated Fractured Rock*, *Geophys. Monogr. Ser.*, vol. 42, edited by D. D. Evans and T. J. Nicholson, pp. 107–114. AGU, Washington, D. C., 1987.

Rice, J. A., *Mathematical Statistics and Data Analysis*, 2nd ed., Duxbury, Boston, Mass., 1995.

Rye, R. R., J. J. A. Mann, and F. G. Yost, The flow of liquids in surface grooves, *Langmuir*, *12*, 555–565, 1996.

Spurk, J. H., *Fluid Mechanics*, Springer-Verlag, New York, 1997.

Thoma, S. G., D. P. Gallegos, and D. M. Smith, Impact of fracture coatings on fracture/matrix flow interactions in unsaturated, porous media, *Water Resour. Res.*, *28*(5), 1357–1367, 1992.

Tokunaga, T. K., and J. Wan, Water film flow along fracture surfaces of porous rock, *Water Resour. Res.*, *33*(6), 1287–1295, 1997.

Tsang, Y. W., and C. F. Tsang, Channel model of flow through fractured media, *Water Resour. Res.*, *23*(3), 467–479, 1987.

Tuller, M., D. Or, and L. M. Dudley, Adsorption and capillary condensation in porous media: Liquid retention and interfacial configurations in angular pores, *Water Resour. Res.*, *35*(7), 1949–1964, 1999.

Wang, J. S. Y., and T. N. Narasimhan, Hydrologic mechanisms governing fluid flow in partially saturated, fractured, porous medium, *Water Resour. Res.*, *21*(12), 1861–1874, 1985.

Zimmerman, R. W., and G. S. Bodvarsson, Hydraulic conductivity of rock fractures, *Transp. Porous Media*, *23*, 1–30, 1996.

D. Or and M. Tuller, Department of Plants, Soils, and Biometeorology, Utah State University, Logan, UT 84322-4820. (dani@tal.agsci.usu.edu; mtuller@mendel.usu.edu)

(Received December 15, 1999; revised January 31, 2000; accepted February 7, 2000.)